

Preview of Comet C/2021 A1 (Leonard) and Its Encounter with Venus

QICHENG ZHANG,¹ QUANZHI YE (叶泉志),² SHREYAS VISSAPRAGADA,¹ MATTHEW M. KNIGHT,³ AND TONY L. FARNHAM²

¹*Division of Geological and Planetary Sciences, California Institute of Technology, Pasadena, CA 91125, USA*

²*Department of Astronomy, University of Maryland, College Park, MD 20742, USA*

³*Department of Physics, United States Naval Academy, Annapolis, MD 21402, USA*

(Received 2021 June 20; Revised 2021 July 20; Accepted 2021 July 24)

ABSTRACT

Long period comet C/2021 A1 (Leonard) will approach Venus to within 0.029 au on 2021 December 18 and may subsequently graze the planet with its dust trail less than two days later. We observed C/2021 A1 with the Lowell Discovery Telescope on 2021 January 13 and March 3, as well as with the Palomar Hale Telescope on 2021 March 20, while the comet was inbound at heliocentric distances of $r = 4.97$ au, 4.46 au, and 4.28 au, respectively. Tail morphology suggests that the dust is optically dominated by ~ 0.1 – 1 mm radius grains produced in the prior year. Neither narrowband imaging photometry nor spectrophotometry reveal any definitive gas emission, placing 3σ upper bounds on CN production of $\lesssim 10^{23}$ molec s^{−1} at both of the latter two epochs. Trajectory analysis indicates that large ($\gtrsim 1$ mm) grains ejected at extremely large heliocentric distances ($r \gtrsim 30$ au) are most strongly favored to reach Venus. The flux of such meteors on Venus, and thus their potential direct or indirect observability, is highly uncertain as the comet’s dust production history is poorly constrained at these distances, but will likely fall well below the meteor flux from comet C/2013 A1 (Siding Spring)’s closer encounter to Mars in 2014, and thus poses negligible risk to any spacecraft in orbit around Venus. Dust produced in previous apparitions will not likely contribute substantially to the meteor flux, nor will dust from any future activity apart from an unlikely high speed ($\gtrsim 0.5$ km s^{−1}) dust outburst prior to the comet reaching $r \approx 2$ au in 2021 September.

Keywords: Comet tails (274) — Long period comets (933) — Meteor trails (1036) — Venus (1763)

1. INTRODUCTION

C/2021 A1 (Leonard) is a long period comet discovered by G. J. Leonard on 2021 January 3 as part of the Catalina Sky Survey (Leonard et al. 2021a). Prediscovery observations were subsequently located to extend the astrometric observation arc back to 2020 April 11 and indicated that it would approach to within 0.029 au of Venus on 2021 December 18 (Leonard et al. 2021b), a distance closer than that of any reliably constrained encounter of a long period comet to Earth.¹ More remarkably, Venus will pass only $\sim 50,000$ km—the *minimum orbit intersection distance* (MOID)—from the comet’s

heliocentric orbit on 2021 December 19 at a point only three days behind the nucleus. This passage is notable because the principal action of solar radiation pressure on dust grains ejected from a comet nucleus is to confine them to a size-sorted dust fan, with the smallest grains (radius $a_d \sim 1$ μ m) rapidly dispersed in the anti-sunward direction and the largest grains ($a_d \gtrsim 1$ mm) more slowly concentrated into a narrow trail along the comet’s heliocentric orbit, lagging behind the nucleus (Finson & Probstein 1968). The exceptionally close approach of Venus to a portion of the comet’s orbit close behind the nucleus therefore raises the possibility that large dust grains from C/2021 A1 may reach Venus to produce a meteor shower.

Meteors are more commonly associated with short period comets, which rapidly fill their physically smaller orbits over many revolutions with dust trails that may be directly observed (e.g., Sykes & Walker 1992) or

Corresponding author: Qicheng Zhang
qicheng@cometary.org

¹ <https://www.minorplanetcenter.net/iau/lists/ClosestComets.html>

otherwise inferred from meteor outbursts when Earth crosses their orbits (e.g., Kresak 1993). Past trails of longer period comets are more sparsely distributed and thinly stretched over their larger orbits, although meteors from such trails are also occasionally detected (e.g., Lyytinen & Jenniskens 2003). Beech (1998), Christou (2010), and others have additionally investigated such periodic meteoroid streams for their potential to generate annual meteor showers on Venus, although such meteor showers have yet to be clearly observed.

Although not a dynamically new comet, C/2021 A1 follows a very large orbit with inbound barycentric semi-major axis $a_{\text{in}} \approx 1900$ au, corresponding to a dynamical lifetime on the order of one orbital period (Królikowska & Dybczyński 2017), which precludes the comet from having developed a discernible, periodic meteoroid stream (Jenniskens et al. 2021). Rather, we are interested in the potential for meteors produced in the ongoing apparition—while the dust is still concentrated behind the nucleus—which is a far more rare occurrence that requires not only a close approach of a comet but one immediately followed by the planet crossing the comet’s orbit behind the nucleus. A nearly as close 0.031 au encounter of C/1983 H1 (IRAS–Araki–Alcock) to Earth—the closest known of a long period comet to Earth—thus produced minimal enhancement in meteor activity, as Earth crossed ahead of rather than behind the nucleus, missing the dust trail (Ohtsuka 1991). Likewise, the 0.07 au encounter of C/1976 E1 (Bradfield) to Venus—the previous closest by a long period comet to Venus reported by JPL SBDB²—likely produced no meteor activity as Venus passed far interior to the comet’s orbit, where no recent dust from the comet could plausibly reach.

Nonetheless, the favorability of C/2021 A1’s encounter with Venus is not unprecedented. Most notably, comet C/2013 A1 (Siding Spring) passed 140,000 km from Mars on 2014 October 19 (Farnocchia et al. 2016). Following this encounter, Mars crossed the dust trail (MOID $\sim 30,000$ km) at a point less than three hours behind the nucleus, intercepting a sizeable fraction of the large, 1–10 mm grains released from the nucleus earlier at a heliocentric distance of $r \sim 22.5$ au (Farnocchia et al. 2014). Ultraviolet spectroscopy by the MAVEN spacecraft in orbit around Mars at the time subsequently revealed the appearance of a temporary metallic vapor layer in the atmosphere with a density consistent with $\sim 10^4$ kg of deposited dust (Schneider et al. 2015), while associated perturbations to the ionosphere were

independently detected by multiple other spacecraft and instruments (Benna et al. 2015; Restano et al. 2015; Sánchez-Cano et al. 2020).

In the following sections, we present early imagery and spectroscopy of C/2021 A1 to provide an initial characterization of the comet and enable a preliminary comparison with other comets. We then discuss the orbital setup, and both the dynamical and physical requirements for dust to reach Venus, and compare these results with those of the prior encounter of C/2013 A1 with Mars. We also briefly speculate on the prospects for detecting meteors on Venus either by direct observation or indirectly through the presence of a meteoritic layer or associated ionospheric perturbations as seen on Mars.

2. OBSERVATIONS

We observed C/2021 A1 with the Lowell Discovery Telescope (LDT) on 2021 January 13 and 2021 March 3 for optical broadband and narrowband imaging, and with the Palomar Hale Telescope (P200) on 2021 March 20 for near-infrared (J) imaging and optical spectroscopy. These observations and the photometry derived from them are summarized in Table 1, with associated images of the comet at all epochs shown in Figure 1.

2.1. Lowell Discovery Telescope (LDT)

We observed the comet using the Large Monolithic Imager (LMI; Massey et al. 2013) on LDT. The LMI has a field of view of $12'.3 \times 12'.3$ and a pixel scale of $0''.36$ after an on-chip 3×3 binning. For the 2021 January 13 run, we collected three usable images through the VR ($V + R$; introduced by Jewitt et al. 1996) filter only, each with 300 s exposure. For the 2021 March 3 run, we collected two sets of images: broadband imagery in r' , as well as narrowband imagery through the CN, BC (blue continuum), and RC (red continuum) filters of the HB set (Farnham et al. 2000). The center wavelength of these filters are 387, 445, and 713 nm, respectively, selected to contain the violet CN ($\Delta v = 0$) emission bands and nearly gas-free continuum points. We began and ended the observation with one 30 s r' image, and cycled through RC, CN and BC three times, with 180 s exposure for each filter each time. This strategy counters brightness variations in time, including from changing airmass and from any passing cirrus, although we note that the sky was clear during the observation. We also dithered the pointing between each exposure in order to mitigate detector defects such as dead pixels and pixel-to-pixel variation.

² <https://ssd-api.jpl.nasa.gov/doc/cad.html>

Table 1. Observations of C/2021 A1

Time (UT)	Instrument	Band	Aperture	Flux (mag) ^a	$Af\rho$ (m)	$A(0^\circ)f\rho$ (m) ^b	Gas Flux (W m ⁻²) ^c	Gas Production (molec s ⁻¹)
2021 Jan 13 ($r = 4.97$ au ^d , $\Delta = 4.71$ au ^e , $\alpha = 11^\circ 2'f$)								
13:01–13:16	LDT/LMI	VR^g	2'' radius	19.4 ± 0.1	2.2 ± 0.2	3.3 ± 0.3
			5'' radius	18.9 ± 0.1	1.3 ± 0.1	2.0 ± 0.2
2021 Mar 3 ($r = 4.46$ au ^d , $\Delta = 3.86$ au ^e , $\alpha = 10^\circ 9'f$)								
08:13–08:43	LDT/LMI	SDSS r'	2'' radius	19.03 ± 0.08	2.0 ± 0.2	3.0 ± 0.3
		HB BC		19.90 ± 0.06	1.7 ± 0.1	2.6 ± 0.2
		HB RC		18.43 ± 0.05	1.9 ± 0.1	2.9 ± 0.1
		SDSS r'	5'' radius	18.46 ± 0.05	1.35 ± 0.07	2.0 ± 0.1
		HB BC		19.26 ± 0.05	1.23 ± 0.06	1.84 ± 0.09
		HB RC		17.74 ± 0.04	1.46 ± 0.06	2.18 ± 0.09
		CN ($\Delta v = 0$) ^h		$<10^{-18.4}$	$<10^{23.0}$
2021 Mar 20 ($r = 4.28$ au ^d , $\Delta = 3.70$ au ^e , $\alpha = 11^\circ 7'f$)								
04:44–05:25	P200/WIRC	2MASS J	2'' radius	17.42 ± 0.06	3.0 ± 0.2	4.6 ± 0.3
			5'' radius	16.88 ± 0.08	2.0 ± 0.2	3.1 ± 0.3
			10'' \times 10''	16.86 ± 0.09	1.8 ± 0.2	2.8 ± 0.3
07:52–08:14	P200/DBSP ⁱ	Bessell B	10'' \times 10''	19.19 ± 0.01	1.13 ± 0.01	1.73 ± 0.01
		Bessell V		18.42 ± 0.01	1.29 ± 0.01	1.99 ± 0.02
		Bessell R		17.98 ± 0.01	1.35 ± 0.01	2.08 ± 0.02
		Bessell I		17.59 ± 0.01	1.42 ± 0.01	2.18 ± 0.02
		SDSS g'		18.80 ± 0.01	1.18 ± 0.01	1.81 ± 0.02
		SDSS r'		18.19 ± 0.01	1.33 ± 0.01	2.05 ± 0.02
		SDSS i'		18.03 ± 0.01	1.38 ± 0.01	2.13 ± 0.02
		HB UC		20.33 ± 0.07	0.97 ± 0.07	1.48 ± 0.10
		HB BC		19.02 ± 0.02	1.14 ± 0.02	1.75 ± 0.03
		HB GC		18.39 ± 0.02	1.29 ± 0.02	1.99 ± 0.04
		HB RC		17.53 ± 0.01	1.37 ± 0.01	2.10 ± 0.02
		CN ($\Delta v = 0$)		20.13 ± 0.05	$<10^{-18.1}$	$<10^{23.3}$
		C ₃ (Swings)		19.59 ± 0.03	$<10^{-17.4}$	$<10^{22.4}$
		C ₂ ($\Delta v = 0$)		18.50 ± 0.02	$<10^{-17.8}$	$<10^{23.0}$

^aNative magnitude for each standard photometric system (SDSS: AB, 2MASS: Vega = 0, Bessell: Vega = 0.03, HB: HD 191263 = 6.19); HB magnitudes before continuum subtraction for gas emission bands.

^bConverted from observed $Af\rho$ with the Schleicher–Marcus phase function (Schleicher & Bair 2011).

^cFull band continuum subtracted gas flux. Upper limits are 3σ .

^dHeliocentric distance.

^eGeocentric distance.

^fPhase angle.

^gCalibrated as SDSS r' .

^hDerived from aperture differencing (see § 2.4), and converted to 5'' radius equivalent aperture.

ⁱRelative uncertainties given for DBSP colors. Absolute flux and $Af\rho$ for stated aperture estimated to be $\pm 5\%$.

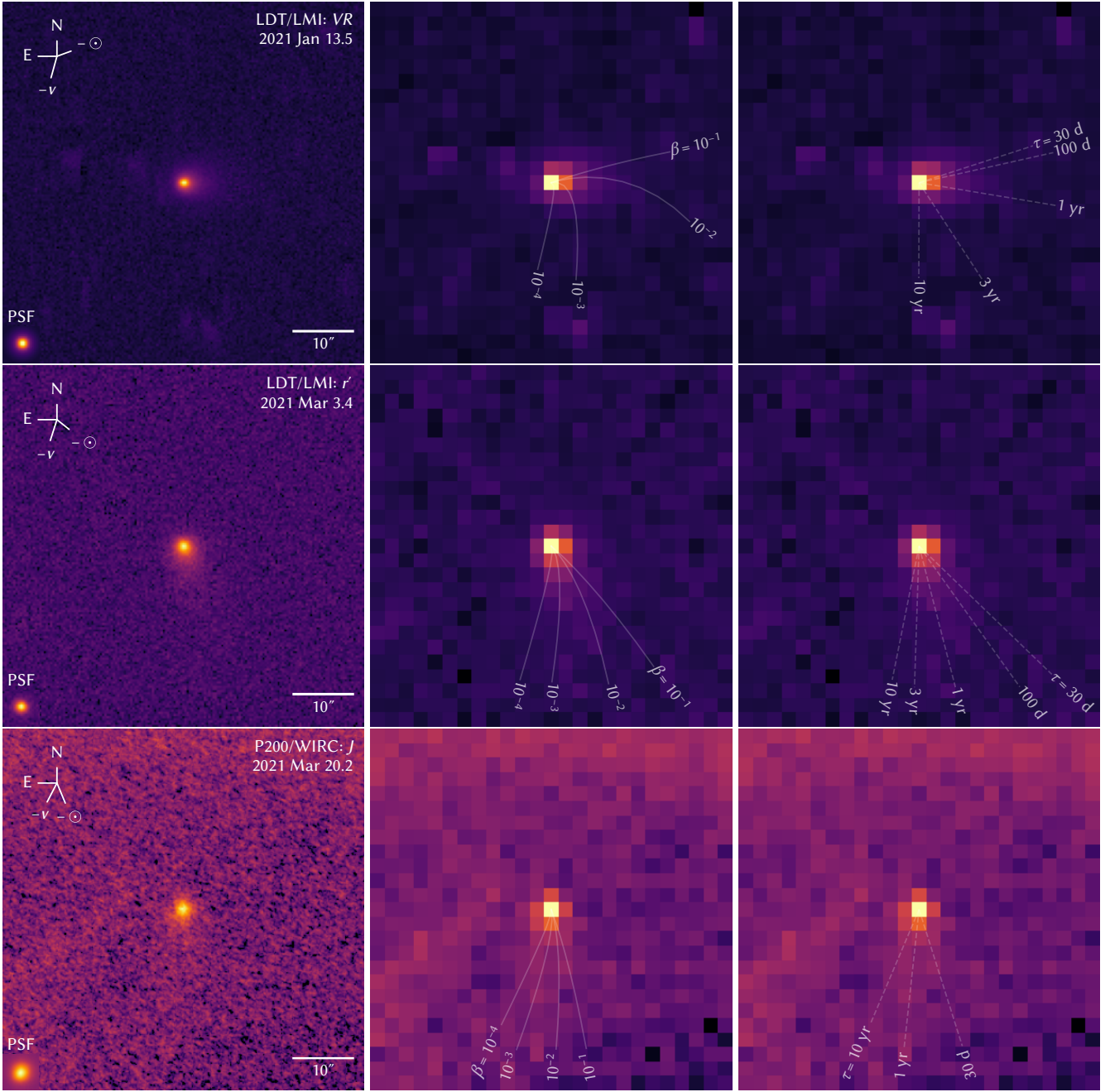


Figure 1. Stacked images from LDT/LMI through the VR filter on 2021 January 13 (top row), through r' on 2021 March 3 (middle row) and from P200/WIRC through J on 2021 March 20 (bottom row). The left panels show the original image with a measured PSF scaled to the brightness of the comet for comparison, and with $-\odot$ and $-v$ indicating the anti-sunward and negative heliocentric velocity directions, respectively. The middle and right panels show the same images binned to $2.4 \text{ arcsec px}^{-1}$ to emphasize the tail. Syndynes (middle) and synchrones (right) are overlaid on both frames, and suggest that the brightness of the tail is predominantly from dust produced within the previous year with $\beta \sim 10^{-2}$ – 10^{-3} , roughly corresponding to $a_d \sim 0.1$ – 1 mm . Note that the $\beta = 1$ syndyne (not plotted) is tightly compressed against the $\beta = 0.1$ syndyne in all epochs, so we cannot exclude a small brightness contribution from $\beta > 0.1$ grains.

We then performed bias subtraction and flat-field correction on the images collected from both nights. Pixels below the 5th and above the 95th percentiles, excluding a region of 5'' in radius centered on the comet (10'' for the *VR* images from 2021 January 13 due to the images being deeper), were masked to remove background stars. Frames were then median-combined into the final stacked images for all filters.

The *VR* and *r'* images were photometrically calibrated using the Pan-STARRS1 DR1 catalog (Chambers et al. 2016), with *VR* approximated as *r'*. The narrowband images were photometrically calibrated using the HB magnitudes of eight field stars computed from their spectra observed by LAMOST (Cui et al. 2012). These HB magnitudes were derived by convolving the transmission profile of each HB filter with the LAMOST spectrum of the star calibrated using the Pan-STARRS1 DR1 catalog, since the LAMOST catalog does not provide absolutely calibrated fluxes. To exclude variable stars and other poor quality spectra, we only used stars with broadband color error—estimated as the standard deviation of the zero-point magnitudes of the spectrum measured for *g'*, *r'*, and *i'*—below 0.1 mag. We also collected images of HB standards during our observation, but encountered unexpected instrumental behavior that prevented us from using these images to perform absolute calibration.

2.2. Palomar Hale Telescope (P200)

We used the Wide-field Infrared Camera (WIRC; Wilson et al. 2003) on P200 to collect *J*-band imagery of the comet. We took 46×60 s exposures spread over a nine-point (3×3) square dither pattern, with a grid spacing of 90''. We performed background subtraction for frames at each dither point by using the median of all frames at the other eight dither positions as the background frame. We then applied flat-field correction with dome flats taken at the beginning of the night, then astrometrically and photometrically solved each frame with field stars from the Gaia EDR3 (Gaia Collaboration et al. 2021) and 2MASS (Skrutskie et al. 2006) catalogs, respectively, before aligning and stacking all frames on the position of the comet.

We also used the Double Spectrograph (DBSP; Oke & Gunn 1982) to collect low resolution spectroscopy of the comet. We used a standard configuration capturing wavelengths of ~ 300 – 550 nm on the blue side and ~ 550 – 1100 nm on the red side, as well as a wide 10'' slit in order to maximize the signal from the comet and improve sensitivity to any diffuse gas emission, and took 4×300 s exposures through both channels. The slit was oriented in the east-west direction, roughly perpendicular to the

tail. As the slit is much wider than the typical atmospheric dispersion over the covered wavelength range, dispersion slit losses are negligible irrespective of slit orientation. We additionally observed the nearby (12° away) spectrophotometric standard star Grw+70 5824 (airmass 1.35) and took 4×60 s exposures with the same configuration immediately prior to observing the comet (airmass 1.14) for flux and sky calibration.

We used PyPeIt (Prochaska et al. 2020) to extract a 10'' wide region centered on the comet for spectrophotometry, corresponding to a $10'' \times 10''$ box aperture. Figure 2 shows the summed and fully calibrated spectrum, binned to 3 nm resolution, as well as an overlay of the slit and extraction aperture over the WIRC image. The solar spectrum of Meftah et al. (2018) is provided as comparison and was divided into the absolute comet spectrum to produce a relative reflectance spectrum. Flux calibration produced a number of artifacts near major telluric absorption features on the red side, likely due to the difference in airmass and brightness profile between the calibration star and comet, and the most prominent of these artifacts have been masked out to aid determination of dust color. A detector artifact on the red camera near 550 nm was also masked out. We used PyPeIt's standard background subtraction routine which measures the sky outside the 10'' extraction box of our C/2021 A1 spectrum, except for the wavelength range 380–520 nm where we instead subtracted a scaled version of the measured Grw+70 5824 sky background in order to avoid subtraction of any spatially extended gas emission in this wavelength range. We do not consider any gas emission features beyond this range, and the contemporaneous imagery shows the dust coma to be clearly contained within the 10'' box, so no features of interest should be included in the subtracted background. Dust colors and gas production limits are discussed further in § 2.3 and § 2.4, respectively.

2.3. Dust Properties

Under the formalism of Finson & Probstein (1968), the spatial position of a dust grain released from the nucleus at zero velocity ($v_d = 0$ m s⁻¹) is uniquely determined by a grid of two properties: (1) the time since the grain was released, τ , and (2) the size parameter β , defined as the ratio of force of solar radiation pressure acting on the grain to that of solar gravitation. For typical low albedo grains of a bulk density $\rho_d \sim 0.5$ g cm⁻³, the effective grain radius a_d is approximately related to β by the inverse relation $a_d \sim 1 \mu\text{m}/\beta$. We note that estimates of the mean ρ_d vary substantially, with values reported in the range of ~ 0.1 – 4 g cm⁻³ (Lasue et al. 2009) with individual comets often producing a

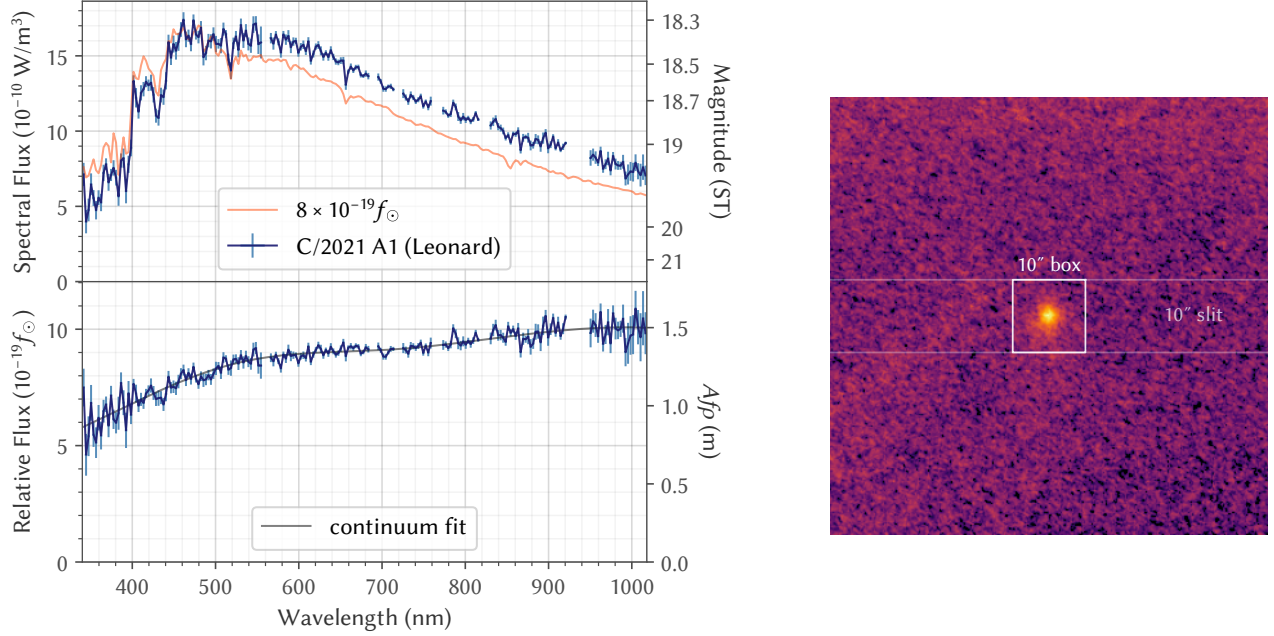


Figure 2. *Left:* Spectrum of C/2021 A1 by P200/DBSP as absolute flux per wavelength interval (top) and relative to the solar spectral flux (bottom), the latter a measure of relative reflectance. The best fit continuum, used for gas production constraints, is also shown for reference. *Right:* Illustration showing the relative size and orientation of the 10'' slit and extraction box aperture overlaid on the P200/WIRC image from Figure 1.

mixture of both compact and fluffy grains (Kolokolova et al. 2018). Differences in ρ_d do not affect our results, except in this rough conversion between β and a_d .

Both stacked images in Figure 1 are accompanied by binned and stretched versions that emphasize the low surface brightness tail, which are overlaid with a selection of *syndynes* and *synchrones*—curves where $v_d = 0$ dust grains of equal β and equal τ fall, respectively. The actual non-zero v_d means the dust with these properties will only approximately fall along these curves, and may be biased to one side by anisotropic dust production, but comparison of tail morphology with respect to the grid of β and τ still enables a useful if rudimentary initial characterization of the dust properties in the tail well away from the coma.

The tail within the observed $\sim 30''$ of the coma is cleanly confined to $\beta > 10^{-4}$, with the surface brightness maximum near $\beta \sim 10^{-2}$ – 10^{-3} at $\tau \lesssim 1$ yr, corresponding to $a_d \sim 0.1$ – 1 mm. This dust is much larger than typically observed from comets nearer to the Sun ($r \sim 1$ au) which are usually brightest in the $\beta \sim 0.1$ – 1 range (Fulle 2004). However, it is comparable with the optically dominant $\beta \sim 10^{-2}$ dust grains observed from other comets at similar r , including C/2013 A1 (Ye & Hui 2014).

We note that the dust that is optically most prominent in the tail is not necessarily representative of the mass distribution of the dust at any point in time. In

particular, while much of the observed $\beta \sim 10^{-2}$ – 10^{-3} dust in the tail was produced at $\tau \sim 1$ yr ($r \sim 8$ au), the larger $\beta \sim 10^{-4}$ dust produced at the same time would still have yet to move out of the coma, and the lower brightness of the tail over this syndyne at similar distances from the coma may merely reflect a lower overall dust production rate at $\tau \gtrsim 10$ yr ($r \gtrsim 30$ au) than at ~ 1 yr, rather than an absence of larger grains being produced. Detailed dust simulations fitted to the surface brightness of the tail are needed to probe these grains, but are beyond the scope of the present analysis.

The spectrum in Figure 2 shows no obvious gas emission lines, so measured colors represent those of the dust. The dust is redder at shorter wavelengths, with a spectral slope of $16\% \pm 3\%$ per 100 nm between the HB BC and GC bands (445–526 nm) dropping to $3\% \pm 1\%$ per 100 nm between GC and RC (526–713 nm). The $B - V = 0.76 \pm 0.01$, $V - R = 0.44 \pm 0.01$, and $R - I = 0.39 \pm 0.01$ derived from the spectrum are nearly indistinguishable from the mean colors reported by Jewitt (2015) for a sample of distant long period comets (0.78 ± 0.02 , 0.47 ± 0.02 , and 0.42 ± 0.03 , respectively). The derived F438W–F606W (438–606 nm) slope of $10\% \pm 1\%$ per 100 nm is also substantially redder than the $5.0\% \pm 0.3\%$ per 100 nm found by Li et al. (2014) for C/2013 A1—a dynamically new comet, unlike C/2021 A1—at similar $r \sim 4$ au.

A'Hearn et al. (1984) introduced the use of the $Af\rho$ parameter as a proxy for the dust production of a comet that requires minimal assumptions about the physical makeup of the dust to compute, unlike the true dust production rate. The $Af\rho$ measured inside a photometric aperture centered on the nucleus is the product of the dust's apparent albedo, A , a filling factor, f , representing the ratio of scattering cross section area to aperture area, and the radius, ρ , of the aperture, and is minimally dependent on ρ for comets with steady state dust production where the dust brightness approximately follows a $1/\rho$ profile.

We measured the $Af\rho$ directly with circular aperture photometry for images from all three epochs. Additionally, although intended for circular apertures, we also estimated the $Af\rho$ over the range of our spectrum in Figure 2 and Table 1 by treating the $10'' \times 10''$ box aperture as equivalent to a $\rho = 5''.7$ circular aperture, as both would capture an identical flux from a $1/\rho$ brightness distribution. We measured $Af\rho$ in $VR \sim r'$ (~ 625 nm) of 1.3 ± 0.1 m on 2021 January 13, and in HB RC (~ 713 nm) of 1.46 ± 0.06 m on 2021 March 3 and 1.37 ± 0.05 m on 2021 March 20 within effective $\rho \approx 5'' \approx 15,000$ km. Since A is strongly dependent on phase angle α , the $Af\rho$ should normally be corrected to the same α before comparison.

We corrected our $Af\rho$ to $\alpha = 0^\circ$ using the Schleicher–Marcus phase function (Schleicher & Bair 2011), as an approximation for the true wavelength dependent phase function of C/2021 A1, and found corresponding $A(0^\circ)f\rho$ of 2.0 ± 0.2 m, 2.2 ± 0.1 m and 2.1 ± 0.1 m in r' within $\rho \approx 5''$ —indistinguishable from constant over our observing period. The $Af\rho$ within a smaller $\rho = 2'' \approx 6,000$ km is ~ 50 – 70% larger in images at all epochs, and likely better reflects the dust production for the extremely small coma that is $< 5''$ in radius for comparison with other comets, but are noisier and more strongly affected by seeing conditions. These $A(0^\circ)f\rho$ values are all several times smaller than the ~ 15 m measured for C/2013 A1 at similar r (Ye & Hui 2014), which—given the fairly similar β of dust observed in the tail—suggests that the dust production of C/2021 A1 is likely lower than that of C/2013 A1 at this distance, although quantitative constraints on the relative dust albedo and size distributions is required to make a definitive conclusion.

2.4. Gas Production

We did not robustly detect any gas emission at either epoch. We used the simple single component model of Haser (1957) to place approximate upper limits on the production of CN, C_3 , and C_2 with a gener-

ous assumed outflow speed of 1 km s^{-1} , and adopted the efficiency factors and scale lengths compiled by A'Hearn et al. (1995), except for the formation length of CN. Fray et al. (2005) notes that breakdown of an unknown parent—possibly dust—is responsible for the short CN formation lengths of $\sim 10^4$ km typically observed and assumed for comets near $r \sim 1$ au, while HCN photodissociation—which has a much longer expected scale length of $\sim 8 \times 10^4 \text{ km} \times (r/1 \text{ au})^2$ (Hänni et al. 2020)—should be the principal source of CN at the $r > 3$ au of our observations, and we adopt this latter value as the formation length of CN in our model. We note that the final production rate estimates increase with increasing formation scale and outflow speed, so an overestimated formation scale and outflow speed provides conservative (i.e., higher) upper limits on gas production.

Since the CN formation scale is larger than the LDT/LMI field-of-view, we adopt the aperture differencing technique described in Ye et al. (2021) to derive the CN production rate from the LDT images. This technique compares the measured difference between two apertures against the modeled value and therefore, relaxes the need to observe a separate background field. After experimenting with apertures of different radii, we used two annuli with inner/outer radii of $10''/15''$ and $45''/60''$ to provide the most stringent constraint. The inner annulus purposely excludes the dust coma to avoid needing a continuum correction. Such a correction would require extrapolating the RC and BC fluxes to the CN bandpass, which is inaccurate if continuum color slope is not constant over the full CN–RC range. We also note that $\sim 60''$ is the largest usable aperture due to uncorrected stray light patterns starting $\sim 90''$ from the nucleus that reach $\sim 1\%$ of the background level. Such patterns were not noted in Ye et al. (2021), likely due to their much shorter exposures and much brighter target. We determined the 3σ upper limit of the excess flux per wavelength interval within the inner annulus above the surface brightness of the outer annulus to be $8.0 \times 10^{-11} \text{ W m}^{-3}$, corresponding to a 3σ CN production limit of $Q(\text{CN}) < 10^{23.0} \text{ molec s}^{-1}$.

We also derived upper limits for CN, C_3 , and C_2 production on 2021 March 20 from the DBSP spectrum. We first used emcee (Foreman-Mackey et al. 2013) to fit a five-point cubic spline function to our reflectance spectrum. To avoid including the gas emission of interest into this fit, we fitted only points in and near the HB continuum bands, and points longward of RC. We approximated the flux uncertainty of all bins as normally distributed and independent, used uniform priors, and verified burn-in completion by visual inspection.

tion of the parameter chains. We then measured the residual flux—accounting for both the flux and continuum uncertainty—through the HB CN, C₃, and C₂ and bandpasses, scaled to the full band CN ($\Delta v = 0$), C₃ (Swings), and C₂ ($\Delta v = 0$) fluxes following Farnham et al. (2000), then converted the 3σ upper bounds to column densities and subsequently production rates by the simple Haser (1957) models described earlier. This procedure yielded 3σ upper bounds of $Q(\text{CN}) < 10^{23.3}$ molec s⁻¹, $Q(\text{C}_3) < 10^{22.4}$ molec s⁻¹, and $Q(\text{C}_2) < 10^{23.0}$ molec s⁻¹, which are roughly equally stringent for typical cometary abundances (A’Hearn et al. 1995).

While no gas emission was detected, we can compare the $Q(\text{CN})$ upper limits with the $A(0^\circ)f\rho = 2.9 \pm 0.1$ m measured by LDT in RC within $\rho = 2''$, and define a ratio $\text{CN}/Af\rho \equiv Q(\text{CN})/(A(0^\circ)f\rho)$ for which we find $\text{CN}/Af\rho < 10^{22.5}$ molec s⁻¹ m⁻¹. This bound is several times smaller than the smallest $\text{CN}/Af\rho$ measured by A’Hearn et al. (1995) after an approximate correction of the latter to 0° phase angle, although the vast majority of measurements were made at much smaller r . Knight & Schleicher (2014) reported a detection of $\text{CN}/Af\rho = 10^{24.1 \pm 0.2}$ molec s⁻¹ m⁻¹ for the dynamically new sungrazing comet C/2012 S1 (ISON) at $r = 4.6$ au pre-perihelion. Similarly, Rauer et al. (1997) found $\text{CN}/Af\rho = 10^{23.5 \pm 0.5}$ molec s⁻¹ m⁻¹ for the very large C/1995 O1 (Hale-Bopp) at $r = 4.6$ au. No measurements of $Q(\text{CN})$ were made of C/2013 A1 until it had already reached $r = 2.4$ au, where Opitom et al. (2016) found $\text{CN}/Af\rho = 10^{24.0 \pm 0.1}$ molec s⁻¹ m⁻¹.

The interpretation and implications of the low $\text{CN}/Af\rho$ observed for C/2021 A1 are unclear without a bigger sample of measurements for comparable long period comets observed at similar r . The absence of the non-HCN parent of CN at $r > 3$ au is likely at least partially responsible. We also speculate that HCN—which sublimates at a lower temperature than H₂O—may be somewhat depleted by thermal fractionation from the outer layers of H₂O ice on the comet, the latter of which may already be weakly sublimating and driving dust production at $r \sim 5$ au (Meech & Svoren 2004). Another possibility is that our $Af\rho$ apertures are sampling an abundance of old, slow-moving grains in the coma and in the portion of the tail behind the coma, thus leading the measured $Af\rho$ to be more reflective of the comet’s accumulated dust production history rather than its ongoing dust production. In all of these cases, we anticipate that $\text{CN}/Af\rho$ will rise to more typical values as the non-HCN source begins to contribute, more efficient H₂O sublimation clears any fractionated layer, old dust grains leave the coma, and changing viewing geometry

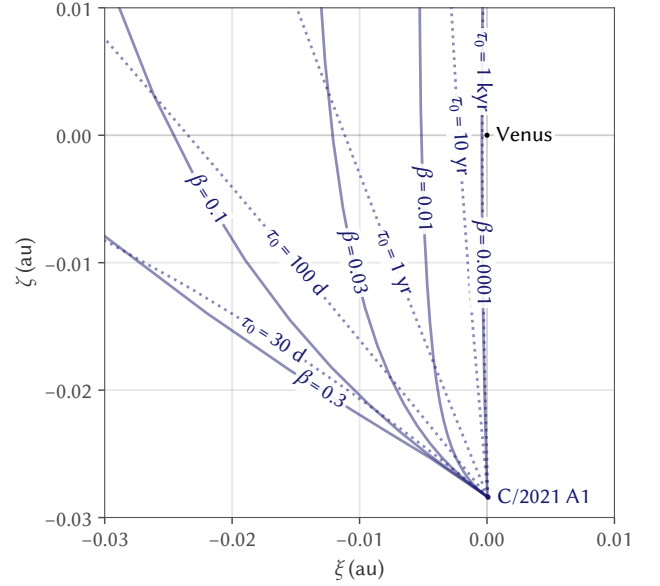


Figure 3. Syndynes (solid curves) and synchrones (dotted curves) of C/2021 A1 projected onto the b -plane of its encounter with Venus, illustrating the closest approach points of $v_d = 0$ dust. Venus falls $\sim 50,000$ km from the edge of this dust fan, so a small but nonzero v_d is required for any dust to reach Venus. Note that the labeled dots indicating the positions of Venus and the nucleus of C/2021 A1 are both much larger than the respective objects, for visibility.

moves the tail out from behind the coma as the comet approaches the Sun.

3. DUST DYNAMICS

The b -plane of a close encounter of a minor to a major planetary body—in our case, C/2021 A1 to Venus—is defined as the plane containing the center of mass of the major body (Venus) that is normal to the inbound asymptotic approach velocity $\mathbf{v}_\infty \equiv v_\infty \hat{\mathbf{v}}_\infty$ of the minor body (C/2021 A1), and serves as a useful tool for describing and analyzing such close encounters (Kizner 1961). We adopted the commonly used formalism of Valsecchi et al. (2003), which labels the plane by two coordinates ξ and ζ associated with the orthonormal unit vectors $\hat{\xi}$ and $\hat{\zeta}$, with Venus at the origin, and with $\hat{\zeta} \times \hat{\xi} = \hat{\mathbf{v}}_\infty$ rotated such that the projected heliocentric velocity of Venus falls along $-\hat{\zeta}$.

Figure 3 shows the b -plane crossing points for dust of several representative β and ejection ages $\tau = \tau_0$ defined from the b -plane crossing time of the nucleus T_0 —effectively the time of its closest approach to Venus (2021 December 18 02:08 UT \pm 3 minutes; JPL orbit solution 9). While each dust grain will technically have a different b -plane, their relative velocity with respect to each other and to the nucleus is much smaller than their

speed with respect to Venus, which ensures that all encounter trajectories are nearly parallel and thus enables the ξ and ζ of their crossing points to be usefully compared together in this manner.

Additionally, the asymptotic approach speed of $v_\infty = 78 \text{ km s}^{-1}$ of C/2021 A1 to Venus is much faster than the escape speed of 10.4 km s^{-1} from the surface of Venus, so gravitational deflection of both the comet nucleus and of all dust grains moving with a similar velocity by Venus will be negligible. In this case, the ξ and ζ where the nucleus and all associated dust grains cross the b -plane represents the spatial position of each respective object's closest approach to the planet. All crossing points $\xi^2 + \zeta^2 \lesssim \tilde{R}_{\text{ven}}^2$ therefore represent impact on the planet, where we have adopted $\tilde{R}_{\text{ven}} = 6200 \text{ km}$ as the solid radius of Venus, plus a $\sim 100 \text{ km}$ buffer as a rough estimate for the portion of atmosphere within which grazing meteors may fully ablate, plus an additional $\sim 50 \text{ km}$ from gravitational focusing of $v_\infty = 78 \text{ km s}^{-1}$ particles by Venus.

As Venus falls just outside the $v_d = 0$ dust fan by the MOID of $\sim 50,000 \text{ km}$, the planet will not encounter an abundance of low v_d dust grains when it crosses the comet's orbital plane and will, instead, only intercept the higher v_d grains that drift to it away from the main fan. To evaluate the plausibility of dust grains reaching Venus, we define a transformation that projects the initial ejection velocity \mathbf{v}_d for each dust grain of β and τ_0 onto its corresponding b -plane crossing point $(\xi, \zeta)(\beta, \tau_0, \mathbf{v}_d)$. This transformation is nearly linear under the linear encounter approximation described above when considering only $(\xi^2 + \zeta^2)^{1/2} \ll 0.7 \text{ au}$ (i.e., Venus' orbit radius), and can therefore be described by (1):

$$\begin{aligned} (\xi, \zeta)(\beta, \tau_0, \mathbf{v}_d) &= (\xi, \zeta)(\beta, \tau_0, \mathbf{0}) + \mathbf{X}_{\beta, \tau_0} \mathbf{v}_d, \\ \mathbf{X}_{\beta, \tau_0} &\equiv \frac{\partial(\xi, \zeta)}{\partial \mathbf{v}_d}(\beta, \tau_0, \mathbf{0}) \end{aligned} \quad (1)$$

Here, $\mathbf{X}_{\beta, \tau_0}$ is a 2×3 Jacobian matrix relating displacements in \mathbf{v}_d to displacements in ξ, ζ . An isotropic shell of dust ejected at equal speed v_d with a given β and τ_0 therefore projects onto a footprint ellipse in the b -plane that is centered on the associated $v_d = 0$ crossing point, with the semiaxes of the ellipse given by v_d multiplied by the singular values of $\mathbf{X}_{\beta, \tau_0}$.

For each β and τ_0 , we compute $(\xi, \zeta)(\beta, \tau_0, \mathbf{0})$ by two body Keplerian trajectories from the comet's heliocentric osculating orbit at T_0 to optimize computing resource usage, and subsequently calculate $\mathbf{X}_{\beta, \tau_0}$ by finite differences. As $a_{\text{in}} \approx 1900 \text{ au}$, this approximation is only valid out to $\sim 1000 \text{ au}$ before the osculating orbit and the true trajectory substantially diverge. Planetary

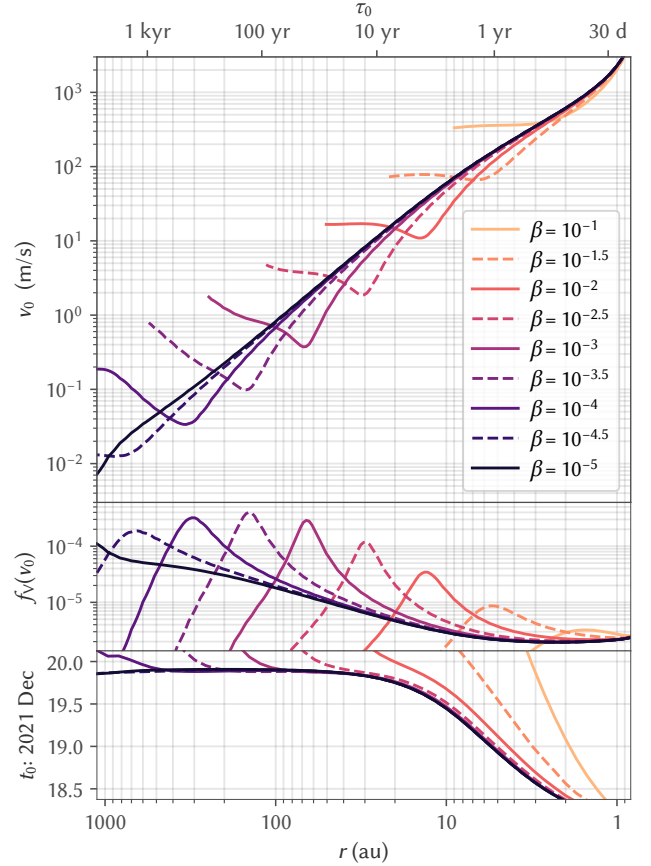


Figure 4. Minimum v_d for dust of various β ejected at various r to reach Venus (v_0), the approximate fraction of dust isotropically ejected with $v_d \sim v_0$ reaching Venus ($f_v(v_0)$), and the time t_0 at which they do so.

perturbations will minimally alter the relative trajectory of the nucleus and dust grains, since all relevant trajectories are tightly clustered together compared to interplanetary distances and thus experience nearly the same perturbations. We then follow Farnocchia et al. (2014) and use Lagrange multipliers to determine the minimum speed $v_d = v_0$ a dust grain with a given β and τ_0 must be ejected with in order to reach Venus, representing a first criterion for any dust grains with a particular set of parameters to become meteors. The first plot of Figure 4 shows that the required v_0 generally decreases with increasing τ_0 , but with each β having an optimum τ_0 where v_0 is minimized, corresponding to the β and τ_0 combinations with $(\xi, \zeta)(\beta, \tau_0, \mathbf{0})$ near the origin. These results and the associated approximations were validated by spot checking with full n -body simulations that include the gravity of the Sun and eight major planets, which indicate the computed \mathbf{v}_0 are generally accurate to within $\sim 10\%$ for $r(\tau_0) \lesssim 30 \text{ au}$, and within a factor of about two for $r(\tau_0) \lesssim 1000 \text{ au}$.

While grains ejected at $v_d > v_0$ in certain directions can reach Venus, only a small fraction of ejected grains will actually do so. This fraction depends on the size of the footprint ellipse, with a larger footprint generally translating to a smaller fraction of dust reaching Venus, once $v_d > v_0$ is met. We consider a meteor production efficiency $f_V(v_0)$ defined as the ratio of $\pi \tilde{R}_{\text{ven}}^2$ to the area of the footprint ellipse for $v_d = v_0$, which very roughly corresponds to the fraction of dust ejected isotropically at $v_d \sim v_0$ that will impact Venus. The second plot of Figure 4 shows that $f_V(v_0)$ is a maximum of $\sim 0.03\%$ for this encounter for dust grains of $\beta \sim 10^{-3}$ – 10^{-4} ejected at $r(\tau_0) \sim 70$ – 300 au with $v_d \sim v_0 \sim 10^{-1} \text{ m s}^{-1}$ —comparable to the escape speed from the surface of a kilometer-scale nucleus. Larger and older grains will generally have even lower v_0 , but which correspond to larger b -plane footprints and thus lower $f_V(v_0)$.

The last plot of Figure 4 shows the impact time t_0 for $v_d = v_0$ dust grains. Meteors associated with distant activity ($\beta \lesssim 10^{-2.5}$, $r(\tau_0) \gtrsim 30$ au)—where efficiency $f_V(v_0) > 0.01\%$ —will largely be concentrated to within ~ 1 h of 2021 December 19 21:00 UT, when Venus passes through its MOID point with the comet’s heliocentric orbit. Any meteors resulting from more recent dust production may begin as soon as ~ 1.5 d earlier near T_0 .

However, no meteors will occur at any time if the comet does not actually produce any dust of $v_d \gtrsim v_0$ on its approach. Dust produced since the comet’s earliest observations at $r = 7.5$ au require a very high $v_d > v_0 > 100 \text{ m s}^{-1}$ to reach Venus. A $\beta = 10^{-2}$ dust grain—near the average observed from C/2021 A1—ejected at $v_d \sim 100 \text{ m s}^{-1}$ in the sunward direction while at $r \sim 5$ – 10 au would experience radiation pressure acceleration relative to the nucleus of $\sim 10^{-6} \text{ m s}^{-2}$ in the anti-sunward direction. The grain would not be turned around and pushed into a tail for > 1 yr while $\gtrsim 10^6$ km from the nucleus. The observed dust coma, however, is two orders of magnitude smaller, yet is already folded into a tail, so we do not observe dust grains ejected near this speed.

Aside from the cases of an extremely large nucleus (Jewitt & Matthews 1999) and near-Sun comets well within the orbit of Venus (Jones et al. 2018)—neither of which apply to C/2021 A1—dust of the observed $\beta \lesssim 10^{-2}$ and needed $v_d > 100 \text{ m s}^{-1}$ are only produced by explosive outbursts where the gas is of sufficient density to accelerate dust to speeds comparable to the outflow speed of up to $\sim 1 \text{ km s}^{-1}$. Such high speed outbursts and the distinctive dust shells morphology they produce are occasionally observed from Jupiter family comets like 15P/Finlay at $r \sim 1$ au (Ye et al. 2015) and

17P/Holmes at 2.4 au (Russo et al. 2008), as well as from active centaurs like 29P/Schwassmann–Wachmann (Trigo-Rodríguez et al. 2008) and 174P/Echeclus (Rousselot 2008) at $r > 5$ au. One such outburst was also observed from the long period comet C/2012 X1 (LINEAR) at 2.7 au (Miles 2013). A dust shell produced by such an outburst from C/2021 A1 expanding at $v_d \gtrsim 0.5 \text{ km s}^{-1}$ can reach Venus if the outburst occurs before the comet reaches $r \approx 2$ au in 2021 September. However, given the exceptional rarity of high speed dust outbursts from long period comets, such an event appears highly unlikely for C/2021 A1. Therefore, neither the comet’s observed past activity nor its future activity are likely to yield any meteors on Venus, and the most likely source for meteors on Venus becomes dust producing activity on the comet from before it was first observed.

Additionally, the comet’s large $a_{\text{in}} \approx 1900$ au implies that perihelion activity from previous apparitions will not substantially affect the meteoroid flux at Venus: Even without non-gravitational forces (i.e., $\beta \rightarrow 0$), particles separated from the nucleus with a modest $v_d = 1 \text{ m s}^{-1}$ at the previous perihelion will be widely spaced along the orbit, preceding or trailing the nucleus by up to ~ 30 kyr in the current apparition. We therefore expect no substantial enhancement in the meteoroid flux near the nucleus from activity on previous apparitions. Any meteor activity observed on Venus from C/2021 A1 would thus most likely originate from distant activity by the comet from earlier in the present apparition.

3.1. Distant Dust Production

Pre-observational distant activity on C/2013 A1 at $r > 10$ au was inferred from the meteor shower it produced on Mars. In that encounter, Mars lay on the b -plane at the intersection of the $\beta = 1.43 \times 10^{-4}$ syndyne and the $r(\tau_0) = 22.5$ au synchrone, and thus efficiently intercepted dust grains produced with these and similar properties (Farnocchia et al. 2014). While the earliest analyses by Vaubaillon et al. (2014) and Moorhead et al. (2014) had suggested that an abundance of younger, high velocity grains could potentially dominate the meteoroid flux at Mars, they required comet behavior ultimately inconsistent with the observed dust production of the comet. Ye & Hui (2014), Tricarico et al. (2014), and Li et al. (2014) directly detected and thus constrained the quantity and velocity of $\beta \lesssim 10^{-2}$ grains produced by the comet, showing that the small and recently produced grains were far too slow to reach Mars. Kelley et al. (2014) likewise simulated dust production starting from $r = 13$ au, showing that there

would be negligible meteor activity from dust produced within this distance.

The remaining possibility of a substantial level of large grains of $\beta \sim 10^{-3}$ – 10^{-4} , or $a_d \sim 1$ – 10 mm, being produced at $r > 10$ au had not been seriously considered prior to the encounter, so the MAVEN IUVS detection of a temporary metallic vapor layer lasting ~ 2 d with a strength consistent with $\sim 10^4$ kg of ablated meteoroids from the comet (Schneider et al. 2015)—far in excess of the layer’s quiescent level (Crismani et al. 2017)—was largely unexpected. Those observations were supplemented by detections of an apparent influx of ions—particularly metallic ions likely of meteoritic origin—into the planet’s ionosphere by instruments aboard MAVEN (Benna et al. 2015), Mars Reconnaissance Orbiter (Restano et al. 2015), and Mars Express (Sánchez-Cano et al. 2020).

We note that Schneider et al. (2015) finds that the high ~ 120 km altitude of the metallic vapor layer—and thus of meteor ablation—to be consistent with predominantly $a_d \sim 1$ – 100 μm meteoroids of $\rho_d < 1$ g cm $^{-3}$, which they suggest implies intercepted grains were actually recently ejected from the nucleus at very high v_d , rather than the expected 1–10 mm grains from $r > 10$ au. However, $\sim 10^4$ kg of grains of $a_d \sim 1$ – 100 μm with typical $\rho_d \sim 0.3$ – 1 g cm $^{-3}$ and $\sim 4\%$ albedo spread over the cross sectional area of Mars would have had a readily observable V-band surface brightness of ~ 21 – 27 mag arcsec $^{-2}$, while telescopic observations of the comet during the encounter were consistent with pre-encounter observations, and revealed no such high v_d dust (Li et al. 2016). Therefore, the intercepted grains were most likely the expected 1–10 mm grains from $r > 10$ au, and we speculate that the high ablation altitude may instead reflect a weaker grain structure that is more prone to fragmentation than exhibited by the much older meteoroids in Earth-crossing streams—which traditional meteor models are largely based on—as such fragile grains in these multi-apparition streams may have already broken down prior to reaching Earth.

Such distant dust activity may not be unusual. More recently, the large Oort cloud comet C/2017 K2 (PANSTARRS) was directly observed to be producing millimeter-sized grains at $r > 20$ au (Hui et al. 2017). This activity appears consistent with surface sublimation of CO (Meech et al. 2017; Jewitt et al. 2019; Yang et al. 2021), a process that can be thermally efficient out to $r \sim 120$ au (Meech & Svoren 2004). Jewitt et al. (2021) concluded from monitoring of the comet’s dust morphology that the observed dust activity was under-

way out at least to $r \approx 35$ au, finding a dust production rate following

$$\dot{m} \approx \dot{m}_{10} \times (10 \text{ au}/r)^2 \quad (2)$$

with $\dot{m}_{10} \sim 1000$ kg s $^{-1}$. They also derive a model for the mean dust ejection speed

$$\langle v_d \rangle \approx v_{10} \times \beta^{0.5} \times (10 \text{ au}/r) \quad (3)$$

and measured $v_{10} \approx 170$ m s $^{-1}$ for C/2017 K2, a value consistent with a $R_{\text{nuc}} \approx 6$ km radius nucleus covered in CO ice, following a theoretical $v_{10} \propto R_{\text{nuc}}^{1/2}$ relation.

C/2021 A1 is intrinsically much fainter than C/2017 K2, and is thus likely to be much smaller, have a much less volatile surface, or both. The dust-contaminated magnitudes reported in the earliest pre-discovery observations (Leonard et al. 2021a) set only a very weak upper bound of $R_{\text{nuc}} \lesssim 7$ km, assuming a typical $\sim 4\%$ albedo. Additionally, the barycentric $a_{\text{in}} \approx 1900$ au suggests the comet has previously survived a perihelion passage of a similar $q \approx 0.6$ au to its present apparition at least once before (Królikowska & Dybczyński 2017), while dynamically new Oort cloud comets of $R_{\text{nuc}} \lesssim 0.5$ km frequently disintegrate at comparable or larger r (e.g., Farnham et al. 2001; Li & Jewitt 2015; Combi et al. 2019). Although we lack a rigorous statistical analysis of survival rate by nucleus size, the survival of C/2021 A1 crudely suggests $R_{\text{nuc}} \gtrsim 0.5$ km, and we adopt $R_{\text{nuc}} \approx 1$ km as the expected value, reflecting both the lower limit and the bottom heavy size distribution of comet nuclei (Boe et al. 2019). This assumed size is additionally comparable to the lower bound of $R_{\text{nuc}} > 0.9$ km obtained by Schleicher et al. (2002) for C/2000 WM $_1$ (LINEAR), a comet with very similar $a_{\text{in}} \approx 1900$ au and $q \approx 0.6$ au to C/2021 A1, as well as a similar brightness at $r \sim 5$ au pre-perihelion.

A nucleus of $R_{\text{nuc}} \approx 1$ km gives $v_{10} \approx 70$ m s $^{-1}$ under Jewitt et al. (2021)’s CO surface sublimation model. This v_{10} implies that a grain of any β ejected at any r in the sunward direction will be turned around by radiation pressure at a distance of $d_{\text{ta}} \sim 80,000$ km away from the nucleus, setting a minimum size for the coma. Figure 1, however, shows a much smaller coma with a sunward edge only $\sim 3''$ from the nucleus in the first epoch, which translates to $d_{\text{ta}} \sim 2000$ km after correcting for the $\alpha \approx 11^\circ$ by approximating the coma as a paraboloid. The small $d_{\text{ta}} \sim 2000$ km corresponds to a much lower $v_{10} \sim 10$ m s $^{-1}$, so the nucleus evidently does not contain large quantities of actively sublimating CO as that of C/2017 K2 appears to have. For comparison, C/2013 A1 was observed to have $v_{10} \sim 20$ m s $^{-1}$ at similar r (Ye & Hui 2014). We note, however, that v_{10}

may have been higher in the past if the $r \sim 5$ au activity is being driven by a less volatile substance like CO_2 or H_2O , or if the surface only became depleted of CO earlier during its present approach to the Sun. The latter could result from seasonal effects if a portion of the nucleus remained shaded through the outbound leg of its previous apparition, and was thus still freshly resurfaced from perihelion until efficient CO sublimation began at $r \sim 120$ au. We therefore regard $v_{10} \approx 70 \text{ m s}^{-1}$ as a plausible albeit unlikely upper limit for dust produced by quiescent surface sublimation.

The first plot of Figure 5 modifies Figure 4 by scaling the calculated v_0 by a factor $\beta^{-0.5}$ to simultaneously compare the necessary v_0 for dust grains of different sizes, since the quantity $v_d \times \beta^{-0.5}$ is approximately independent of β under the model in (3). The plot shows that the $v_{10} \approx 70 \text{ m s}^{-1}$ of a CO-covered surface at $r < 120$ au is nearly the minimum required for dust of any size released by the comet at any point on its current apparition to have the needed $v_d \geq v_0$ to reach Venus. The second plot shows the corresponding f_V for the footprint ellipse set by $v_{10} = 70 \text{ m s}^{-1}$, which is a rough approximation of the dust ejected under this model of a given τ_0 and β that impact Venus. We also consider $v_d \times \beta^{-0.5}$ to be lognormally distributed about the nominal value, with a geometric standard deviation σ^* , and select a plausible $\sigma^* = 1.2$ for this figure. The true σ^* is affected by many factors, including the distribution of particle drag coefficients and nucleus non-uniformity, and a precise computation is beyond the scope of this analysis. We also consider a dust mass production rate of $\dot{m}_{10} = 1 \text{ kg s}^{-1}$ with (2) for the third plot, which shows the mass $m_V(<\beta)$ of all dust grains larger than the indicated β reaching Venus under this model produced per unit interval of $\ln r$, denoted by $r \times \partial_r m_V(<\beta)$. The plot shows that these meteoroids intercepted by Venus will be principally by $\beta \sim 10^{-3}$ grains produced near $r \sim 100$ au around the maximum r where efficient CO sublimation is possible.

As $v_{10} = 70 \text{ m s}^{-1}$ is very near the threshold speed for any dust to reach Venus, the cumulative mass of meteoroids intercepted by Venus $m_V(\text{CO})$ under this CO sublimation model is extremely sensitive to the precise values of v_{10} and σ^* . Figure 6 plots the intercepted mass $m_V(\text{CO})$ and corresponding mass flux $\dot{m}_V(\text{CO})$ for a variety of v_{10} and σ^* for the adopted $\dot{m}_{10} = 1 \text{ kg s}^{-1}$. A substantial meteoroid flux at Venus occurs only for high $v_{10} \gtrsim 70 \text{ m s}^{-1}$ or high $\sigma^* \gtrsim 1.2$, which will produce $m_V(\text{CO}) \sim 10^2 \text{ kg}$ of meteors on Venus. We note that the model treats dust as non-interacting particles that can be linearly superposed, so the results may be scaled to any \dot{m}_{10} by $m_V(\text{CO}) \propto \dot{m}_{10}$. However, if the

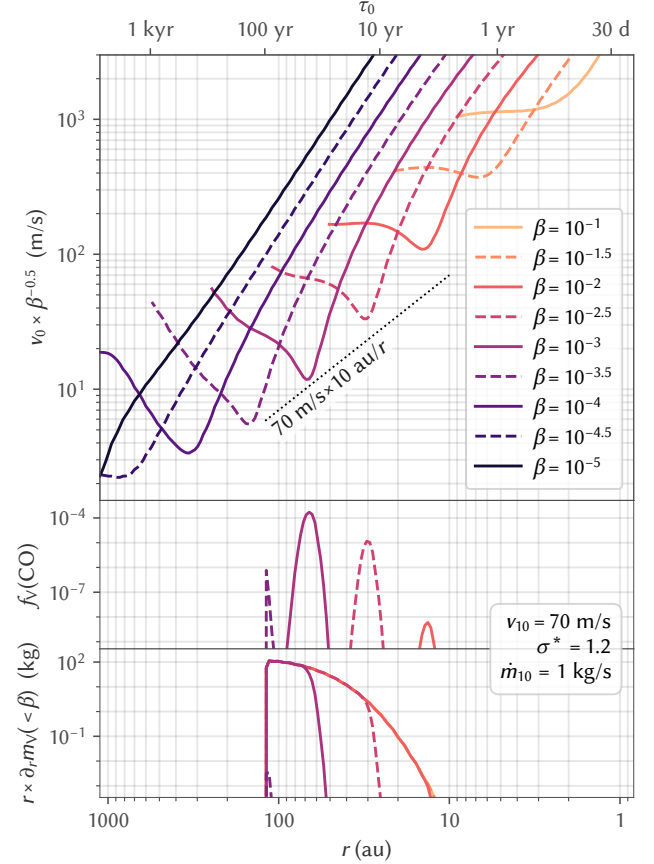


Figure 5. The v_0 from Figure 4 scaled by $\beta^{-0.5}$ relative to the $v_{10} = 70 \text{ m s}^{-1}$ for a 2 km diameter nucleus with CO surface sublimation, the fraction $f_V(\text{CO})$ of such dust intercepted by Venus, and the intercepted mass m_V below the indicated β produced per unit interval of $\ln r$ —denoted by $r \times \partial_r m_V(<\beta)$ —serving as a rough approximation for the intercepted mass produced near r .

$v_{10} \sim 10 \text{ m s}^{-1}$ observed near $r \sim 5$ au held throughout its approach, the comet will produce negligible meteor activity on Venus without an exceptionally high $\sigma^* \gtrsim 2$ where a substantial fraction of dust is ejected at several times the nominal speed. In contrast, an equivalent model for C/2013 A1’s encounter with Mars—where Mars actually passed within the $v_d = 0$ dust fan—gives the observed $\sim 10^4 \text{ kg}$ of meteors for the adopted $\dot{m}_{10} \sim 1 \text{ kg s}^{-1}$ at all reasonable v_{10} and σ^* , indicating that CO surface sublimation adequately explains the meteor activity on Mars from C/2013 A1.

Distant activity may also be driven by mechanisms other than the quiescent surface sublimation we have modeled. For example, [Sekanina & Kracht \(2014\)](#) note that C/2012 S1 was trailed by a stream of dust extending several degrees behind the nucleus, which syndyne-synchrone analysis indicates were comprised of $\beta \lesssim 10^{-3}$

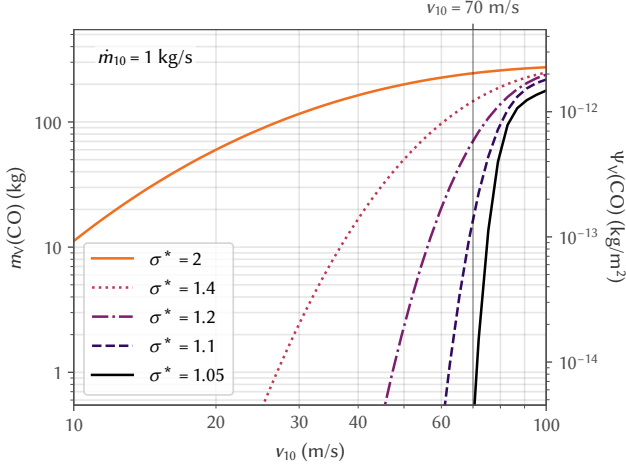


Figure 6. Total mass $m_V(\text{CO})$ and mass flux density $\Psi_V(\text{CO})$ intercepted by Venus as functions of typical normalized dust ejection speed v_{10} and geometric dust speed dispersion σ^* for isotropic dust production $\dot{m} \propto r^{-2}$ and $\dot{m}_{10} \equiv \dot{m}(10 \text{ au}) = 1 \text{ kg s}^{-1}$ from the CO sublimation limit $r = 120 \text{ au}$ to 10 au .

grains ejected at $r \gtrsim 10 \text{ au}$, and suggests based on the sublimation behavior that it may have contained pebbles of $\beta \sim 10^{-4}$ from as far as $r \sim 100 \text{ au}$ produced by annealing of amorphous ice. DiSanti et al. (2016) and Feldman et al. (2018) found the comet had a low $Q(\text{CO})/Q(\text{H}_2\text{O}) \sim 1.5\%$ near $r \sim 1 \text{ au}$, which suggests that CO surface sublimation was unlikely to have been responsible for the distant activity, unless the surface abundance of CO was considerably higher earlier.

Extremely distant activity has also been inferred from the trajectories of fragmented comets. The comet pair C/1988 F1 (Levy) and C/1988 J1 (Holt) were discovered following nearly the same orbit spaced only 76 d apart—too close for the progenitor to have split on its previous apparition, yet too far to have split after entering the planetary region on its current apparition (Marsden 1988). Simulations by Sekanina & Kracht (2016) suggest the pair likely separated at $\sim 1 \text{ m s}^{-1}$ centuries earlier at $r \sim 300\text{--}900 \text{ au}$, already on its approach to perihelion. Likewise, the arrival clustering of the Kreutz sungrazing comet family appears to require its members to split decades before perihelion at $r \gtrsim 50 \text{ au}$ and $\sim 10 \text{ m s}^{-1}$ (Sekanina & Chodas 2004).

The physical mechanisms behind the distant fragmentation events are unclear, and no obvious large fragments or companions to C/2021 A1 have been discovered as of 2021 May. However, if such mechanisms are present that can split comets several tens or even hundreds of astronomical units before perihelion at $\sim 1\text{--}10 \text{ m s}^{-1}$, it seems plausible that they may, under other circumstances that may or may not apply to C/2021 A1, propel

smaller, unseen fragments or large dust grains from the comet at similar r with the $v_d \geq v_0 \sim 0.1\text{--}1 \text{ m s}^{-1}$ necessary to reach Venus. Without a clear physical explanation for this behavior, however, we cannot meaningfully speculate on the likelihood of such activity contributing substantially to the meteoroid flux at Venus.

3.2. Meteor Observability

Venus’ MOID point passage near 2021 December 19 21:00 UT, when large, distantly released meteoroids from C/2021 A1 are most favored to reach the planet, will occur while Earth is only 0.32 au away. From Earth, Venus will have an apparent diameter of $53''$ at 28° solar elongation with a thin crescent illuminated at 140° phase angle. Meteors from the comet will approach the planet at $v_\infty = 78 \text{ km s}^{-1}$ from directions tightly clustered within a few arcminutes of the radiant at R.A. $10^{\text{h}}52^{\text{m}}$ and decl. $+36^\circ55'$ (J2000), prior to gravitational focusing. This radiant is overhead from a sub-radiant point at longitude 353° and latitude $+27^\circ$, which is on both the Earth-facing and nightside hemispheres near the evening terminator. Figure 7 plots contours of radiant zenith angle over the apparent disk and illuminated crescent of Venus viewed from Earth, indicating the portion of the disk where meteors from the comet, if any, are likely to appear.

At a distance of 0.32 au, meteors on Venus will be $\sim 28 \text{ mag}$ fainter than a terrestrial meteor of the same intrinsic brightness observed from a typical $\sim 100 \text{ km}$ away. A 0.5 m aperture telescope and detector with a system throughput of 30% under ideal sky conditions is sensitive to point sources out to $V \sim 16$ in exposures as short as $\sim 0.1 \text{ s}$, corresponding to Venus meteors of $V \sim -12$ from $\sim 100 \text{ km}$ away. While terrestrial meteors from solar system comets are never as fast as the $v_\infty = 78 \text{ km s}^{-1}$ expected for C/2021 A1 meteors on Venus, Leonid meteors are nearly so, at $v_\infty = 71 \text{ km s}^{-1}$, so serve as reasonably close analogs, although C/2021 A1 meteors of the same mass will be $\sim 20\%$ more energetic and additionally brighter from the shorter scale height in Venus’ upper atmosphere (Christou 2004; McAuliffe & Christou 2006). Leonids of $V \sim -12$ are not uncommon and may be produced by meteoroids of $\sim 0.2 \text{ kg}$ in mass, which have $\beta \sim 10^{-5}$ (Shrbený & Spurný 2009). No dust with $\beta \lesssim 10^{-3.5}$ produced by surface sublimation of CO can reach Venus, so other mechanisms—such as those responsible for the distant pre-perihelion splitting of C/1988 F1 and C/1988 J1, and of the Kreutz sungrazers, as discussed in the previous section—are required to produce any meteors bright enough to be observed on Venus from Earth.

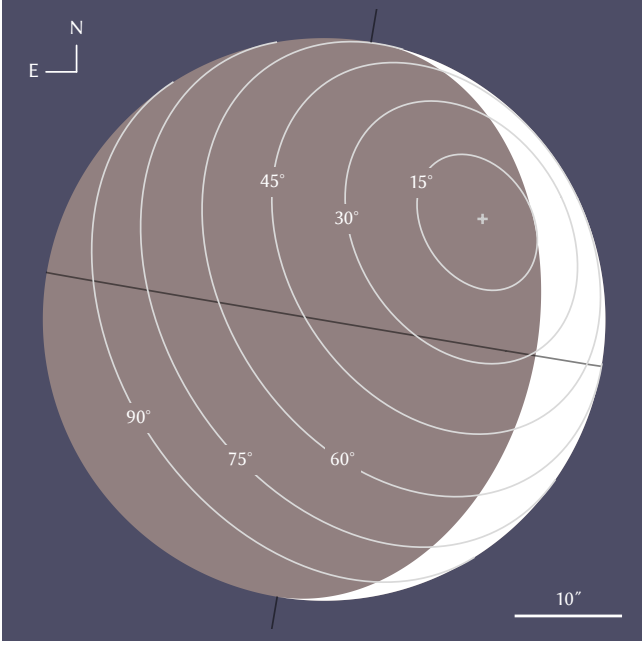


Figure 7. Spatial map for potential meteors on Venus viewed from Earth at 2021 December 19 21:00 UT: Contours indicate curves of constant radiant zenith angle, and encircle the subradiant point (marked by “+”). Dark lines indicate Venus’ equator and axis of rotation, while the white crescent represents the solar illuminated portion of the planet. Meteors are possible anywhere on the disk the zenith angle is $<90^\circ$, but are most probable near the subradiant point.

In practice, $V \sim 16$ serves as an optimistic limit given that any meteors must be observed in close proximity to Venus’ brilliantly illuminated dayside, and coronagraphic optics like those developed to search for lightning on the nightside may be required to approach this limit (e.g., [Hansell et al. 1995](#)). Bandpass filters encompassing select bright meteor emission features, such as the Na I D lines at 589.0/589.6 nm or the O I line at 777 nm ([Carbary et al. 2004](#)), may further aid in stray light and background rejection. Additionally, the low elongation of Venus means any observations will be limited to high airmass in twilight, while the short window of no more than ~ 2 h for bright meteors associated with distant activity geographically restricts any such observations to a narrow corridor through the Atlantic Ocean and the easternmost portions of Canada and Brazil.

Fluorescence from a meteoritic metallic vapor layer, like that detected by [Schneider et al. \(2015\)](#) on Mars following the C/2013 A1 encounter, may also be observable near the terminator—particularly near the northern limb, where apparent column density is elevated by foreshortening. One appealing candidate is Na I, whose D lines are readily observable from the ground, and for which a persistent meteoritic layer of 10^{13} –

10^{14} atoms m^{-2} is well-observed over Earth (e.g., [Cabbannes et al. 1938](#); [Chapman 1939](#); [Chamberlain 1956](#)). As on Earth, Venus’ low heliocentric radial velocity of -0.2 km s^{-1} during the encounter combined with the deep Na I D Fraunhofer absorption lines in the solar spectrum strongly suppresses the intensity of the resonance emission, with a fluorescence efficiency of ~ 1 photon s^{-1} atom $^{-1}$ for the D2 (589.0 nm) line. Keck HIRES spectroscopy has been demonstrated to be sensitive to emission lines on Venus down to a vertical equivalent $\sim 20 \text{ R}$ ([Slanger et al. 2001](#)), and other large telescopes equipped with echelle or Fabry–Pérot etalon spectrographs with spectral resolving power $\gtrsim 50,000$ that can cleanly distinguish Venusian emission lines from telluric lines—separated by 8.3 km s^{-1} in radial velocity—may be similarly sensitive. This limit translates to $\sim 2 \times 10^{11}$ atoms m^{-2} of Na I, or the typical Na content of $\sim 200 \text{ kg}$ of ablated meteoritic material distributed over one hemisphere of Venus in the absence of ionization or other upper atmospheric chemical reactions that may remove Na I. We note, however, that Venus lacks a persistent Na I layer like Earth’s, suggesting that Na I is indeed rapidly consumed by atmospheric chemistry ([Krasnopol’sky 1983](#)). A more careful analysis is required to evaluate if meteoritic Na I can sufficiently persist for $\gtrsim 1 \text{ h}$ (i.e., at least through the end of the meteor shower) for any plausible mass of ablated meteoritic material to be detected in this manner.

Additionally, the Akatsuki orbiter remains in operation around Venus ([Nakamura et al. 2011](#)), and will likely be the only spacecraft in the immediate vicinity of the planet during the C/2021 A1 encounter; no flybys of Venus are planned for Parker Solar Probe³, Solar Orbiter⁴, or BepiColombo⁵ within one month of the event. Absent an extreme level of distant activity by unknown mechanisms or severe violations of our defined assumptions, the encounter poses negligible risk to spacecraft health. Even an enormous $\dot{m}_{10} \sim 1000 \text{ kg}$ from CO surface sublimation comparable to that of C/2017 K2 and $\sim 1000\times$ larger than inferred for C/2013 A1 will produce a meteoroid fluence of $\lesssim 10^{-3}$ particles m^{-2} at Venus for all plausible values of v_{10} and σ^* .

Akatsuki, however, may have the capability to observe any meteors and their subsequent effects on Venus. Of note, Akatsuki carries a Lightning and Airglow Camera

³ <http://parkersolarprobe.jhuapl.edu/The-Mission/index.php#Timeline>

⁴ <https://sci.esa.int/web/solar-orbiter/-/44181-mission-operations>

⁵ <https://sci.esa.int/web/bepicolombo/-/48871-getting-to-mercury>

(LAC; Takahashi et al. 2018) that monitors for lightning at the 777 nm O I line that is also a strong meteor emission feature, and thus should be sensitive to bright meteors. However, LAC is only operational for 20–30 minutes per 10 d orbit when the Sun is fully eclipsed by Venus from the spacecraft, so the camera is unlikely to be operable during the brief window of possible meteor activity from C/2021 A1. Akatsuki also carries an Ultraviolet Imager (UVI; Yamazaki et al. 2018) which includes a 283 nm channel covering the Mg II resonance lines at 279.6/280.3 nm that are among the brightest emission features of terrestrial meteors (Carbary et al. 2004) and were also the brightest lines observed in the C/2013 A1 meteoritic layer on Mars (Schneider et al. 2015). UVI can integrate for up to 11 s per exposure, and may be useful for directly imaging bright meteors during the encounter as well as to constrain the brightness of any Mg II layer above the twilight limb afterward, although the wide 14 nm bandpass means such observations will likely be strongly impacted by stray light originating from the illuminated dayside if not performed in eclipse. Finally, features in the ionospheric electron density profile have been characterized as meteoritic ion layers (Pätzold et al. 2009; Withers et al. 2013), and Akatsuki’s Radio Science (RS; Imamura et al. 2017) radio occultation experiment may be sensitive to large perturbations to these layers comparable to that observed by similar methods during C/2013 A1’s encounter with Mars (Restano et al. 2015; Sánchez-Cano et al. 2020).

4. CONCLUSIONS

The upcoming encounter of C/2021 A1 to Venus is among the closest known of a long period comet to any planet, and is surpassed in recent history only by the 2014 encounter of C/2013 A1 to Mars, which produced a meteor shower on the planet that was indirectly observed by multiple spacecraft. To help ascertain the potential for meteors on Venus, we collected imagery and spectroscopy of C/2021 A1 following its discovery, in advance of the encounter. We found the comet’s dust color and size to be typical of other dynamically old long period comets at its distance, with the tail optically dominated by $a_d \sim 0.1\text{--}1$ mm grains produced within the prior year. Our nondetection of CN sets an upper limit of $\text{CN}/A_f\rho < 10^{22.5}$ molec $\text{s}^{-1} \text{m}^{-1}$ that is considerably lower than values typically reported; however, few such measurements have been reported at the $r = 4\text{--}5$ au of our observations, so the low $\text{CN}/A_f\rho$ may not necessarily be abnormal for comets at this distance.

Trajectory analysis shows that—barring an unlikely $v_d \gtrsim 0.5$ km s^{-1} outburst before the comet reaches $r \approx 2$ au in 2021 September—large dust grains of

$a_d \gtrsim 1$ mm released at $r \gtrsim 30$ au are dynamically most strongly favored to reach Venus, but cometary dust production behavior at such large r is poorly constrained. These large grains inefficiently scatter light, and their presence in the dust trail cannot be usefully constrained telescopically. Quiescent surface sublimation of CO beginning as far as $r \sim 120$ au can plausibly produce $a_d \sim 1$ mm dust grains that become meteors on Venus, but likely requires the nucleus to have had a much greater abundance of near-surface CO than the minute coma we observed suggests is presently accessible. Other distant activity mechanisms, such as those responsible for splitting comet nuclei hundreds of astronomical units away, could potentially produce larger meteors on Venus, the brightest of which may be directly observable from Earth around 2021 December 19 20–22:00 UT. As with C/2013 A1’s Mars encounter, the aftermath of a particularly strong meteor shower can also be detected through the formation of a meteoritic metallic vapor layer and through perturbations to the ionosphere, from Earth and/or by the Akatsuki orbiter around Venus. We encourage observations of this event to take advantage of the rare opportunity to probe an otherwise unseen dust trail, and subsequently constrain cometary behavior at distances where no comets have ever been observed.

We thank Michael S. P. Kelley and Lori M. Feaga for help with collecting observations, Ludmilla Kolokolova for discussions on the properties of cometary dust grains, and an anonymous referee for helpful comments and suggestions in their review of this manuscript. We additionally thank Joel Pearman, Kevin Rykowski, and Carolyn Heffner for observing support with the Palomar Hale Telescope, as well as Sydney Perez and Ana Hayslip for their support with the Lowell Discovery Telescope.

This research makes use of observations from the Hale Telescope at Palomar Observatory, which is owned and operated by Caltech and administered by Caltech Optical Observatories.

These results made use of the Lowell Discovery Telescope (LDT) at Lowell Observatory. Lowell is a private, non-profit institution dedicated to astrophysical research and public appreciation of astronomy and operates the LDT in partnership with Boston University, the University of Maryland, the University of Toledo, Northern Arizona University and Yale University. The University of Maryland observing team consisted of Quanzhi Ye, James Bauer, Michaela Blain, Adeline Gicquel-Brodtke, Tony Farnham, Lori Feaga, Michael Kelley, and Jessica Sunshine.

This research has made use of data and/or services provided by the International Astronomical Union’s Minor Planet Center.

This work was supported by NSF award AST1852589. S. V. is supported by an NSF Graduate Research Fellowship and the Paul & Daisy Soros Fellowship for New Americans.

Facilities: DCT (LMI), Hale (DBSP, WIRC)

Software: Astropy (Astropy Collaboration et al. 2013), emcee (Foreman-Mackey et al. 2013), Matplotlib (Hunter 2007), NumPy (Van Der Walt et al. 2011), PyeIt (Prochaska et al. 2020), sbpy (Mommert et al. 2019)

REFERENCES

- A’Hearn, M. F., Millis, R. C., Schleicher, D. G., Osip, D. J., & Birch, P. V. 1995, *Icar*, 118, 223
- A’Hearn, M. F., Schleicher, D., Millis, R., Feldman, P., & Thompson, D. 1984, *AJ*, 89, 579
- Astropy Collaboration, Robitaille, T. P., Tollerud, E. J., et al. 2013, *A&A*, 558, A33
- Beech, M. 1998, *MNRAS*, 294, 259
- Benna, M., Mahaffy, P., Grebowsky, J., et al. 2015, *GeoRL*, 42, 4670
- Boe, B., Jedicke, R., Meech, K. J., et al. 2019, *Icar*, 333, 252
- Cabannes, J., Dufay, J., & Gauzit, J. 1938, *ApJ*, 88, 164
- Carbary, J., Morrison, D., Romick, G., & Yee, J. 2004, *ASR*, 33, 1455
- Chamberlain, J. W. 1956, *JATP*, 9, 73
- Chambers, K., Magnier, E., Metcalfe, N., et al. 2016, *arXiv:1612.05560*
- Chapman, S. 1939, *ApJ*, 90, 309
- Christou, A. 2010, *MNRAS*, 402, 2759
- Christou, A. A. 2004, *Icar*, 168, 23
- Combi, M. R., Mäkinen, T., Bertaux, J.-L., et al. 2019, *ApJL*, 884, L39
- Crismani, M. M., Schneider, N. M., Plane, J. M., et al. 2017, *NatGe*, 10, 401
- Cui, X.-Q., Zhao, Y.-H., Chu, Y.-Q., et al. 2012, *RAA*, 12, 1197
- DiSanti, M., Bonev, B., Gibb, E., et al. 2016, *ApJ*, 820, 34
- Farnham, T. L., Schleicher, D. G., & A’Hearn, M. F. 2000, *Icar*, 147, 180
- Farnham, T. L., Schleicher, D. G., Woodney, L. M., et al. 2001, *Sci*, 292, 1348
- Farnocchia, D., Chesley, S. R., Chodas, P. W., et al. 2014, *ApJ*, 790, 114
- Farnocchia, D., Chesley, S. R., Micheli, M., et al. 2016, *Icar*, 266, 279
- Feldman, P. D., Weaver, H. A., A’Hearn, M. F., Combi, M. R., & Russo, N. D. 2018, *AJ*, 155, 193
- Finson, M., & Probst, R. 1968, *ApJ*, 154, 327
- Foreman-Mackey, D., Hogg, D. W., Lang, D., & Goodman, J. 2013, *PASP*, 125, 306
- Fray, N., Bénilan, Y., Cottin, H., Gazeau, M.-C., & Crovisier, J. 2005, *P&SS*, 53, 1243
- Fulle, M. 2004, in *Comets II*, ed. M. C. Festou, H. U. Keller, & H. A. Weaver (Univ. of Arizona Press), 565–576
- Gaia Collaboration, Brown, A. G., Vallenari, A., et al. 2021, *A&A*
- Hänni, N., Altwegg, K., Pestoni, B., et al. 2020, *MNRAS*, 498, 2239
- Hansell, S., Wells, W., & Hunten, D. 1995, *Icar*, 117, 345
- Haser, L. 1957, *BSRSL*, 43, 740
- Hui, M.-T., Jewitt, D., & Clark, D. 2017, *AJ*, 155, 25
- Hunter, J. D. 2007, *CSE*, 9, 90
- Imamura, T., Ando, H., Tellmann, S., et al. 2017, *EP&S*, 69, 1
- Jenniskens, P., Lauretta, D. S., Towner, M. C., et al. 2021, *Icar*, 365, 114469
- Jewitt, D. 2015, *AJ*, 150, 201
- Jewitt, D., Agarwal, J., Hui, M.-T., et al. 2019, *AJ*, 157, 65
- Jewitt, D., Kim, Y., Mutchler, M., et al. 2021, *AJ*, 161, 188
- Jewitt, D., Luu, J., & Chen, J. 1996, *AJ*, 112, 1225
- Jewitt, D., & Matthews, H. 1999, *AJ*, 117, 1056
- Jones, G. H., Knight, M. M., Battams, K., et al. 2018, *SSRv*, 214, 20
- Kelley, M. S., Farnham, T. L., Bodewits, D., Tricarico, P., & Farnocchia, D. 2014, *ApJL*, 792, L16
- Kizner, W. 1961, *P&SS*, 7, 125
- Knight, M. M., & Schleicher, D. G. 2014, *AJ*, 149, 19
- Kolokolova, L., Nagdimunov, L., & Mackowski, D. 2018, *JQSRT*, 204, 138
- Krasnopol’sky, V. 1983, in *Venus*, ed. D. M. Hunten, L. Colin, & T. M. Donahue (Univ. of Arizona Press), 459–483
- Kresak, L. 1993, *A&A*, 279, 646
- Królikowska, M., & Dybczyński, P. A. 2017, *MNRAS*, 472, 4634
- Lasue, J., Levasseur-Regourd, A. C., Hadamcik, E., & Alcouffe, G. 2009, *Icar*, 199, 129
- Leonard, G., Aschi, S., Pettarin, E., et al. 2021a, *MPEC*, 2021-A99
- . 2021b, *CBET*, 4907

- Li, J., & Jewitt, D. 2015, *AJ*, 149, 133
- Li, J.-Y., Samarasinha, N. H., Kelley, M. S., et al. 2014, *ApJL*, 797, L8
- . 2016, *ApJL*, 817, L23
- Lyytinen, E., & Jenniskens, P. 2003, *Icar*, 162, 443
- Marsden, B. 1988, *BAAS*, 20, 898
- Massey, P., Dunham, E., Bida, T., et al. 2013, *AAS*, 221, 345.02
- McAuliffe, J. P., & Christou, A. A. 2006, *Icar*, 180, 8
- Meech, K., & Svoren, J. 2004, in *Comets II*, ed. M. C. Festou, H. U. Keller, & H. A. Weaver (Univ. of Arizona Press), 317–336
- Meech, K. J., Kleyana, J. T., Hainaut, O., et al. 2017, *ApJL*, 849, L8
- Meftah, M., Damé, L., Bolsée, D., et al. 2018, *A&A*, 611, A1
- Miles, R. 2013, *JBAA*, 123, 363
- Mommert, M., Kelley, M., de Val-Borro, M., et al. 2019, *JOSS*, 4
- Moorhead, A. V., Wiegert, P. A., & Cooke, W. J. 2014, *Icar*, 231, 13
- Nakamura, M., Imamura, T., Ishii, N., et al. 2011, *EP&S*, 63, 443
- Ohtsuka, K. 1991, in *Origin and Evolution of Interplanetary Dust*, ed. A. C. Levasseur-Regourd & H. Hasegawa (Springer), 315–318
- Oke, J., & Gunn, J. 1982, *PASP*, 94, 586
- Opitom, C., Guilbert-Lepoutre, A., Jehin, E., et al. 2016, *A&A*, 589, A8
- Pätzold, M., Tellmann, S., Häusler, B., et al. 2009, *GRL*, 36
- Prochaska, J. X., Hennawi, J. F., Westfall, K. B., et al. 2020, *JOSS*, 5, 2308
- Rauer, H., Arpigny, C., Boehnhardt, H., et al. 1997, *Sci*, 275, 1909
- Restano, M., Plaut, J. J., Campbell, B. A., et al. 2015, *GRL*, 42, 4663
- Rousselot, P. 2008, *A&A*, 480, 543
- Russo, N. D., Vervack Jr, R., Weaver, H., et al. 2008, *ApJ*, 680, 793
- Sánchez-Cano, B., Lester, M., Witasse, O., et al. 2020, *JGRA*, 125, e2019JA027344
- Schleicher, D. G., & Bair, A. N. 2011, *AJ*, 141, 177
- Schleicher, D. G., Woodney, L. M., & Birch, P. V. 2002, in *Cometary Science after Hale-Bopp* (Springer), 401–403
- Schneider, N. M., Deighan, J., Stewart, A., et al. 2015, *GeoRL*, 42, 4755
- Sekanina, Z., & Chodas, P. W. 2004, *ApJ*, 607, 620
- Sekanina, Z., & Kracht, R. 2014, *arXiv:1404.5968*
- . 2016, *ApJ*, 823, 2
- Shrbený, L., & Spurný, P. 2009, *A&A*, 506, 1445
- Skrutskie, M., Cutri, R., Stiening, R., et al. 2006, *AJ*, 131, 1163
- Slanger, T., Cosby, P., Huestis, D., & Bida, T. 2001, *Sci*, 291, 463
- Sykes, M. V., & Walker, R. G. 1992, *Icar*, 95, 180
- Takahashi, Y., Sato, M., Imai, M., et al. 2018, *EP&S*, 70, 1
- Tricarico, P., Samarasinha, N. H., Sykes, M. V., et al. 2014, *ApJL*, 787, L35
- Trigo-Rodríguez, J., García-Melendo, E., Davidsson, B., et al. 2008, *A&A*, 485, 599
- Valsecchi, G. B., Milani, A., Gronchi, G. F., & Chesley, S. R. 2003, *A&A*, 408, 1179
- Van Der Walt, S., Colbert, S. C., & Varoquaux, G. 2011, *CSE*, 13, 22
- Vaubailion, J., Maquet, L., & Soja, R. 2014, *MNRAS*, 439, 3294
- Wilson, J. C., Eikenberry, S. S., Henderson, C. P., et al. 2003, *Proc. SPIE*, 4841, 451
- Withers, P., Christou, A., & Vaubailion, J. 2013, *ASR*, 52, 1207
- Yamazaki, A., Yamada, M., Lee, Y. J., et al. 2018, *EP&S*, 70, 1
- Yang, B., Jewitt, D., Zhao, Y., et al. 2021, *arXiv:2105.10986*
- Ye, Q., Knight, M. M., Kelley, M. S., et al. 2021, *PSJ*, 2, 23
- Ye, Q.-Z., Brown, P. G., Bell, C., et al. 2015, *ApJ*, 814, 79
- Ye, Q.-Z., & Hui, M.-T. 2014, *ApJ*, 787, 115